Journal of Power Sources 224 (2013) 99–114

Contents lists available at SciVerse ScienceDirect

Journal of Power Sources

journal homepage: www.elsevier.com/locate/jpowsour

Analysis of cold start processes in proton exchange membrane fuel cell stacks

Yueqi Luo, Qian Guo, Qing Du, Yan Yin, Kui Jiao*

State Key Laboratory of Engines, Tianjin University, 92 Weijin Rd, Tianjin 300072, China

HIGHLIGHTS

- A 3D multiphase model is developed to study the cold start process of PEMFC stacks.
- Stacks with more cells can reach higher temperature with better performance.
- Ice formation in middle cells is slower.

ARTICLE INFO

Article history:
Received 28 June 2012
Received in revised form
24 September 2012
Accepted 26 September 2012
Available online 3 October 2012

Keywords:
Proton exchange membrane fuel cell
Stack
Cold start
Three-dimensional multiphase model
Ice formation

ABSTRACT

To comprehensively understand the cold start processes of proton exchange membrane fuel cell (PEMFC) stack which is important for the automotive applications, a three-dimensional multiphase PEMFC stack model is developed in this study. The detailed analysis of the cold start processes shows that for the stacks with more cells, the voltage decreases more slowly due to the lower ice formation rates. The temperature increases faster for a stack with more cells, and a higher temperature can be reached at the end of the cold start process. No apparent difference in voltage exists among the different individual cells in a stack when the reactant gases are evenly supplied to each cell. The temperature in the individual cell in the middle of a stack is higher and more evenly distributed than those on the sides and single cells, due to weakened cooling effect of the bi-polar plate (BP) on the membrane electrode assembly (MEA), and the ice formation rate is also lower in the middle cell. At a lower current density, the ice in the cathode catalyst layer (CL) is formed faster at the section close to the BP, and it is close to the membrane at a higher current density.

© 2012 Elsevier B.V. All rights reserved.

1. Introduction

Proton exchange membrane fuel cell (PEMFC) is one of the promising clean and efficient power sources for transportation applications, owing to its high power density, low temperature operation and zero/low emission [1]. Start-up of PEMFC stack from sub-zero temperatures has been recognized to be an essential issue before its successful commercialization. Several countries and regions have set specific targets for cold start performance. For example, in the United States, the latest target was set by the Department of Energy (DOE), which requires unassisted successful start-up from −40 °C [2], a much more difficult requirement than the one established in 2005. The European Union sets several general technical targets for the years 2015–2020, including the lowest successful cold start temperature of −25 °C, and well maintained proton conductivity at low temperatures (over 10 mS cm^{-1} at −20 °C) [3]. The Japanese government has also established a series of programs, and in recent years, the main plan has been shifted from “strategic development” to “commercialization promotion” [4], indicating that the focus of research and development is now on the commercially applied fuel cell stacks. As for fuel cell manufacturers, the General Motors Corporation set the target of unassisted start-up from −40 °C as well [5].

A number of experimental studies have been conducted to investigate the cold start performance and characteristics of PEMFCs [6–18]. The focus has been on the measurement of general performance behaviors, performance degradation and visualization of ice formation during cold start processes. Cold start models have also been developed for single cells [19–24] and stacks [25–27] in an effort to better understand the start-up process. Single cell analytical models have been mainly targeted to discover the relationship between the design/operating parameters and cold start performance [19–21], and most of these models have only considered either individual components (e.g. cathode catalyst layer (CL)) [19] or simplified cells (one-dimensional models) [20,21]. Multiphase multi-dimensional numerical simulations have been carried out for single PEMFCs to investigate more detailed transport processes [22–24]. Mao et al. [22] found that ice in the cathode CL appears first at the flow channel inlet region and extends

* Corresponding author. Tel.: +86 22 87402029; fax: +86 22 27406949.
E-mail address: kjiao@tju.edu.cn (K. Jiao).

0378-7753/$ – see front matter © 2012 Elsevier B.V. All rights reserved.
http://dx.doi.org/10.1016/j.jpowsour.2012.09.089

Nomenclature

A	stack geometric area, m^2
c	molar concentration, mol m^{-3}
C_p	specific heat, J kg^{-1} K^{-1}
D	mass diffusivity, m^2 s^{-1}
EW	equivalent weight of membrane, 1100 kg $kmol^{-1}$
F	Faraday's constant, 96,487 C mol^{-1}
h	latent heat, J kg^{-1}; heat transfer coefficient, W m^{-2} K^{-1}
I	current density, A cm^{-2}
j	reaction rate, A m^{-3}
k	thermal conductivity, W m^{-1} K^{-1}
K	permeability, m^2
$\dot{m}$	mass flow/transfer rate, kg s^{-1}
M	molecular weight, kg $kmol^{-1}$
p	pressure, Pa
q	heat flux, W m^{-2}
$\dot{Q}$	heat transfer rate, W
RH	relative humidity
s	volume fraction
S	source terms, entropy, J $kmol^{-1}$ K^{-1}
t	time, s
T	temperature, K or °C
$\vec{u}$	velocity, m s^{-1}
x	mole fraction
Y	mass fraction

Greek letters

α	transfer coefficient
ε	porosity
η	overpotential, V
ι	interfacial drag coefficient
κ	electrical conductivity, S m^{-1}
λ	water content in ionomer
μ	dynamic viscosity, kg m^{-1} s^{-1}
ξ	stoichiometry ratio
ρ	density, kg m^{-3}
ϕ	electrical potential, V
ω	volume fraction of ionomer in catalyst layer

Subscripts and superscripts

a	anode
act	activation
BP	bi-polar plate
c	cathode
CL	catalyst layer
cond	condensation
desb	desublimation
eff	effective
ele	electronic
equil	equilibrium
EOD	electro-osmotic drag
evp	evaporation
f	frozen
fl	fluid phase
fmw	frozen membrane water
fusn	fusion
FPD	freezing point depression
g	gas phase
GDL	gas diffusion layer
H_2	hydrogen
H_2O	water
i	the ith components or the ith cell in a stack
ice	ice
in	inlet
init	initial condition
ion	ionic
lq	liquid water
m	mass (for source term)
melt	melt
mem	membrane
N	total number of cells in a stack, normal condition
nf	non-frozen
nmw	non-frozen membrane water
O_2	oxygen
out	outlet
pc	phase change
ref	reference state
sat	saturation
sl	solid phase
stk	stack characteristic
surr	surroundings
T	energy (for source term)
u	momentum (for source term)
vp	water vapor
wall	surrounding wall of the single cell or stacks
0	intrinsic value
l-i	liquid water to ice (vice versa)
n-f	non-frozen membrane water to frozen membrane water (vice versa)
n-i	non-frozen membrane water to ice
n-v	non-frozen membrane water to vapor (vice versa)
v-i	vapor to ice
v-l	vapor to water liquid (vice versa)

toward the outlet region gradually, the start-up current density influences the water uptake potential of the membrane, and a lower current density is beneficial for water uptake. Meng [23] predicted that the cold start process obtains a benefit from the higher gas flow rates in the cathode flow channel. Jiao and Li [24] found that it is favorable to increase the ionomer fraction in the cathode CL, and a thinner membrane enhances the water uptake rate.

In order to supply sufficient power for vehicles, individual PEMFCs are often assembled in series to form stacks. Interactions between the individual cells in a stack become significant, making the cold start characteristics of PEMFC stacks different from single cells [16]. Sundaresan and Moore [25] developed a layered cold start stack model, which considered the water phase change and the thermal effects, and this model predicted the temperature of different cells in a stack. A one-dimensional model developed by Khandelwal et al. [26] also obtained the temperature distribution in a PEMFC stack. Based on this model, several assisted start-up strategies were tested and compared. Ahluwalia and Wang [27] developed a two-dimensional cold start stack model, and the ice formation was considered in this model. It was found that a high current density is favorable for rapid cold start of PEMFC stacks, and the metal bi-polar plates (BPs) are better than graphite to improve the cold start abilities due to the lower heat capacity of metal. The PEMFC cold start related studies were also reviewed recently in detail by Meng and Ruan [28] and Jiao and Li [29].

As mentioned above, most of the previous cold start models only considered single cells and one-dimensional/two-dimensional approach to stack level. To comprehensively understand the PEMFC stack cold start processes, a three-dimensional multiphase PEMFC stack model is needed. In this study, a three-dimensional

multiphase PEMFC stack model is developed, and the cold start processes of PEMFC stacks are investigated numerically. This article is organized as follows: the stack model is presented first, followed by the results and discussion, and finally the conclusion is given.

2. Stack model

2.1. Physical problem

The computational domain of this model is based on practical PEMFC stacks with typical components, including the BPs with flow channels machined on them and the membrane electrode assemblies (MEAs). To save the computational time, a 50 mm straight segment of each cell in the stacks are considered, which consists of one of the parallel channels as well as the certain part of BPs, gas diffusion layers (GDLs), CLs and membranes. The stack component properties and operating conditions are shown in Table 1, and the computational domain and mesh for a three-cell stack considered in this study are shown in Fig. 1. With more computational power and time, stacks with more individual cells and larger reaction areas can also be simulated by using this model with general formulations.

2.2. Assumptions

A number of assumptions are made for this stack model:

(1) The flow is laminar due to the low Reynolds number.
(2) Isotropic material properties are considered.
(3) All the gas species are ideal gas.
(4) Water exists in the ionomer as non-frozen membrane water and frozen membrane water, in the pores of CL and GDL as vapor, liquid and ice, and the amount of liquid water in flow channel is fixed at zero because it can be removed quickly in the short and straight flow channels considered in this study.
(5) The product water from the electrochemical reaction is absorbed by the ionomer in the cathode CL immediately, thus in the non-frozen membrane water state.
(6) The different phases (gas, liquid and solid) are at local thermodynamic equilibrium such that they share the same temperature at the same grid point, therefore a single energy conservation equation is solved in this model.

2.3. Conservation equations

Mass conservation of gas mixture:

$$\frac{\partial}{\partial t}\left(\varepsilon\left(1-s_{\mathrm{lq}}-s_{\mathrm{ice}}\right)\rho_{\mathrm{g}}\right)+\nabla\cdot\left(\rho_{\mathrm{g}}\vec{u}_{\mathrm{g}}\right)=S_{\mathrm{m}} \tag{1}$$

where S_{m} (kg m^{-3} s^{-1}) is the source term:

$$S_{\mathrm{m}}=S_{\mathrm{H_2}}+S_{\mathrm{O_2}}+S_{\mathrm{vp}} \tag{2}$$

The first term on the right hand side of Equation (2) represents the hydrogen consumption in anode CL; the second term is for the oxygen consumption in cathode CL; and the third term accounts for the phase change related to water vapor:

$$S_{\mathrm{H_2}}=\begin{cases}-\dfrac{j_{\mathrm{a}}}{2F}M_{\mathrm{H_2}} & (\text{in anode CL})\\ 0 & (\text{in other zones})\end{cases} \tag{3}$$

$$S_{\mathrm{O_2}}=\begin{cases}-\dfrac{j_{\mathrm{c}}}{4F}M_{\mathrm{O_2}} & (\text{in cathode CL})\\ 0 & (\text{in other zones})\end{cases} \tag{4}$$

$$S_{\mathrm{vp}}=\begin{cases}-S_{\mathrm{v\text{-}l}}-S_{\mathrm{v\text{-}i}}+S_{\mathrm{n\text{-}v}}M_{\mathrm{H_2O}} & (\text{in CL})\\ -S_{\mathrm{v\text{-}l}}-S_{\mathrm{v\text{-}i}} & (\text{in GDL})\end{cases} \tag{5}$$

The corresponding source terms for water condensation/evaporation ($S_{\mathrm{v\text{-}l}}$, kg m^{-3} s^{-1}), desublimation ($S_{\mathrm{v\text{-}i}}$, kg m^{-3} s^{-1}), and ionomer hydration/dehydration due to water vapor ($S_{\mathrm{n\text{-}v}}$, kg m^{-3} s^{-1}) are

$$S_{\mathrm{v\text{-}l}}=\begin{cases}\begin{cases}\gamma_{\mathrm{cond}}\varepsilon\left(1-s_{\mathrm{lq}}-s_{\mathrm{ice}}\right)\dfrac{\left(p_{\mathrm{g}}X_{\mathrm{vp}}-p_{\mathrm{sat}}\right)M_{\mathrm{H_2O}}}{RT} & \left(\text{if } p_{\mathrm{g}}X_{\mathrm{vp}}\geq p_{\mathrm{sat}}\right)\\ \gamma_{\mathrm{evap}}\varepsilon s_{\mathrm{lq}}\dfrac{\left(p_{\mathrm{g}}X_{\mathrm{vp}}-p_{\mathrm{sat}}\right)M_{\mathrm{H_2O}}}{RT} & \left(\text{if } p_{\mathrm{g}}X_{\mathrm{vp}}<p_{\mathrm{sat}}\right)\end{cases} & (\text{if } T\geq T_{\mathrm{N}}+T_{\mathrm{FPD}})\\ 0 & (\text{if } T<T_{\mathrm{N}}+T_{\mathrm{FPD}})\end{cases} \tag{6}$$

Table 1
Stack properties and operating conditions.

Parameter	Value
Channel length; width; depth; rib width	50; 1.0; 1.0; 1.0 mm
Thicknesses of membrane (Nafion 112); CL; GDL	0.051; 0.01; 0.2 mm
Densities of membrane; CL; GDL; BP	$\rho_{\mathrm{men,CL,GDL,BP}}=1980;1000;1000;1000\ \mathrm{kg\ m^{-3}}$
Specific heat capacities of membrane; CL; GDL; BP	$(C_p)_{\mathrm{men,CL,GDL,BP}}=833;3300;568;1580\ \mathrm{J\ kg^{-1}\ K^{-1}}$
Thermal conductivities of membrane; CL; GDL; BP	$k_{\mathrm{men,CL,GDL,BP}}=0.95;1.0;1.0;20\ \mathrm{W\ m^{-1}\ K^{-1}}$
Electric conductivities of CL; GDL; BP	$\kappa_{\mathrm{CL,GDL,BP}}=300;300;20,000\ \mathrm{S\ m^{-1}}$
Volume fraction of ionomer (ω) in CL, and the porosities (ε) of CL; GDL	$\omega=0.2$; $\varepsilon_{\mathrm{CL,GDL}}=0.3;0.6$
Intrinsic permeabilities of CL; GDL	$K^0_{\mathrm{CL}}=6.2\times10^{-13}\ \mathrm{m^2}$; $K^0_{\mathrm{GDL}}=6.2\times10^{-12}\ \mathrm{m^2}$
Current densities (galvanostatic)	$I=0.05\ \mathrm{A\ cm^{-2}}$ or $0.1\ \mathrm{A\ cm^{-2}}$
Stoichiometry ratio	$\xi_{\mathrm{a,c}}=2.0$
Relative humidities of inlet gases	$\mathrm{RH}^{\mathrm{in}}_{\mathrm{a,c}}=0$
Inlet gas and surrounding temperatures	$T^{\mathrm{in}}_{\mathrm{a,c}}=T_{\mathrm{surr}}=-20\ ^\circ\mathrm{C}$
Pressure at outlets	$p^{\mathrm{out}}_{\mathrm{a,c}}=1\ \mathrm{atm}$
Initial stack temperature	$T_{\mathrm{stk,init}}=T_{\mathrm{surr}}=-20\ ^\circ\mathrm{C}$
Heat transfer coefficients on outside surface	$h=50\ \mathrm{W\ m^{-2}\ K^{-1}}$
Initial ice volume fraction in the cell	0
Initial non-frozen water content in the membrane and CLs and frozen water content in the membrane	5; 0

$$S_{\text{v-i}} = \begin{cases} \begin{cases} \gamma_{\text{desb}}\varepsilon\left(1-s_{\text{lq}}-s_{\text{ice}}\right)\dfrac{\left(p_{\text{g}}X_{\text{vp}}-p_{\text{sat}}\right)M_{\text{H}_2\text{O}}}{RT} & \left(\text{if } p_{\text{g}}X_{\text{vp}} \geq p_{\text{sat}}\right) \\ 0 \quad \left(\text{if } p_{\text{g}}X_{\text{vp}} < p_{\text{sat}}\right) \end{cases} & (\text{if } T < T_{\text{N}} + T_{\text{FPD}}) \\ 0 & (\text{if } T \geq T_{\text{N}} + T_{\text{FPD}}) \end{cases} \tag{7}$$

$$S_{\text{n-v}} = \xi_{\text{n-v}}\frac{\rho_{\text{mem}}}{\text{EW}}\left(\lambda_{\text{nf}}-\lambda_{\text{equil}}\right)\left(1-s_{\text{lq}}-s_{\text{ice}}\right) \tag{8}$$

Momentum conservation of gas mixture:

$$\begin{aligned} &\frac{\partial}{\partial t}\left(\frac{\rho_{\text{g}}\vec{u}_{\text{g}}}{\varepsilon\left(1-s_{\text{lq}}-s_{\text{ice}}\right)}\right) + \nabla\cdot\left(\frac{\rho_{\text{g}}\vec{u}_{\text{g}}\vec{u}_{\text{g}}}{\varepsilon^2\left(1-s_{\text{lq}}-s_{\text{ice}}\right)^2}\right) = \\ &-\nabla p_{\text{g}} + \mu_{\text{g}}\nabla\cdot\left(\nabla\left(\frac{\vec{u}_{\text{g}}}{\varepsilon\left(1-s_{\text{lq}}-s_{\text{ice}}\right)}\right) + \nabla\left(\frac{\vec{u}_{\text{g}}^{\text{T}}}{\varepsilon\left(1-s_{\text{lq}}-s_{\text{ice}}\right)}\right)\right) \\ &-\frac{2}{3}\mu_{\text{g}}\nabla\left(\nabla\cdot\left(\frac{\vec{u}_{\text{g}}}{\varepsilon\left(1-s_{\text{lq}}-s_{\text{ice}}\right)}\right)\right) + S_{\text{u}} \end{aligned} \tag{9}$$

and the source term in this equation is:

$$S_{\text{u}} = \begin{cases} -\dfrac{\mu_{\text{g}}}{K_{\text{g}}}\vec{u}_{\text{g}} & (\text{in CL and GDL}) \\ 0 & (\text{in other zones}) \end{cases} \tag{10}$$

where the μ_{g} (kg m^{-1} s^{-1}) is the dynamic viscosity of the gas mixture, $\vec{u}_{\text{g}}$ (m s^{-1}) the gas phase superficial velocity vector, and K_{g} (m^2) the gas phase permeability.

Mass conservation of gas species (i: hydrogen, oxygen and water vapor):

$$\frac{\partial}{\partial t}\left(\varepsilon\left(1-s_{\text{lq}}-s_{\text{ice}}\right)\rho_{\text{g}}Y_i\right) + \nabla\cdot\left(\rho_{\text{g}}\vec{u}_{\text{g}}Y_i\right) = \nabla\cdot\left(\rho_{\text{g}}D_i^{\text{eff}}\nabla Y_i\right) + S_i \tag{11}$$

and the source term in the above equation represents the source terms of hydrogen, oxygen and water vapor conservation equations, as given in Equations (3)–(5). The effect of ice blockage on the diffusion of reactant in electrode is also considered:

$$D_i^{\text{eff}} = D_i\varepsilon^{1.5}\left(1-s_{\text{lq}}-s_{\text{ice}}\right)^{1.5} \tag{12}$$

Mass conservation of liquid water:

$$\frac{\partial\left(\varepsilon s_{\text{lq}}\rho_{\text{lq}}\right)}{\partial t} + \nabla\cdot\left(\iota\rho_{\text{lq}}\vec{u}_{\text{g}}\right) = \nabla\cdot\left(\rho_{\text{lq}}D_{\text{lq}}\nabla s_{\text{lq}}\right) + S_{\text{lq}} \tag{13}$$

where the source term S_{lq} (kg m^{-3} s^{-1}) includes the water evaporation/condensation and freezing/melting:

$$S_{\text{lq}} = S_{\text{v-l}} - S_{\text{l-i}} \tag{14}$$

where $S_{\text{l-i}}$ (kg m^{-3} s^{-1}) represents water freezing/melting:

$$S_{\text{l-i}} = \begin{cases} \gamma_{\text{fusn}}\varepsilon s_{\text{lq}}\rho_{\text{lq}} & (\text{if } T < T_{\text{N}} + T_{\text{FPD}}) \\ -\gamma_{\text{melt}}\varepsilon s_{\text{ice}}\rho_{\text{ice}} & (\text{if } T \geq T_{\text{N}} + T_{\text{FPD}}) \end{cases} \tag{15}$$

The water phase change is also related to the Gibbs–Thompson undercooling effect, and more detailed discussions on the water phase change considered in this model can be found in Ref. [24].

Mass conservation of ice:

$$\frac{\partial(\varepsilon s_{\text{ice}}\rho_{\text{ice}})}{\partial t} = S_{\text{ice}} \tag{16}$$

where the source term considering the various water phase changes is

$$S_{\text{ice}} = \begin{cases} S_{\text{v-i}} + S_{\text{l-i}} + S_{\text{n-i}}M_{\text{H}_2\text{O}} & (\text{in CL}) \\ S_{\text{v-i}} + S_{\text{l-i}} & (\text{in GDL}) \end{cases} \tag{17}$$

where $S_{\text{n-i}}$ (kg m^{-3} s^{-1}) represents the process that non-frozen membrane water in CL freezes to ice:

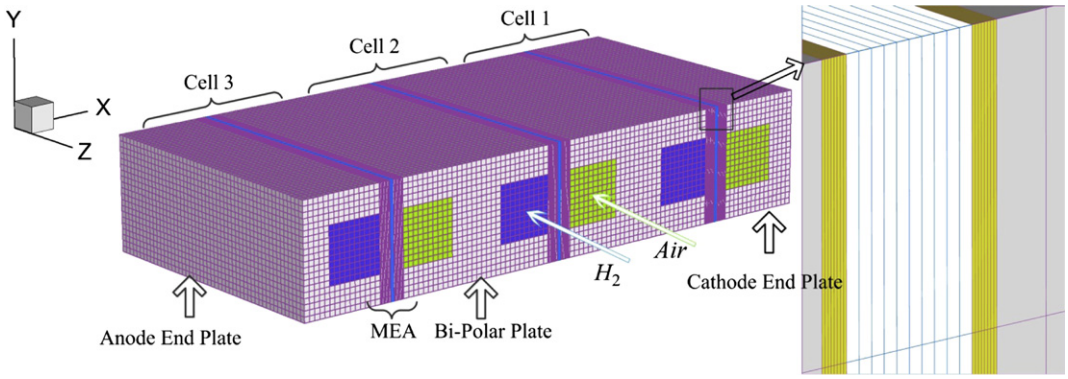

Fig. 1. Computational domain and mesh (individual cells in the three-cell stack are marked as Cell 1, Cell 2 and Cell 3 from the cathode side to the anode side).

$$S_{\text{n-i}} = \begin{cases} \xi_{\text{n-i}} \dfrac{\rho_{\text{mem}}}{\text{EW}} \left(\lambda_{\text{nf}} - \lambda_{\text{sat}}\right)\left(1 - s_{\text{lq}} - s_{\text{ice}}\right) & \left(\text{if } \lambda_{\text{nf}} \geq \lambda_{\text{sat}}\right) \\ 0 & \left(\text{if } \lambda_{\text{nf}} < \lambda_{\text{sat}}\right) \end{cases} \tag{18}$$

This is based on the assumption that in CL, the non-frozen membrane water may freeze, and the formed ice appears in the pores of CL directly [24].

Mass conservation of non-frozen membrane water:

$$\frac{\rho_{\text{mem}}}{\text{EW}} \frac{\partial\left(\omega\lambda_{\text{nf}}\right)}{\partial t} = \frac{\rho_{\text{mem}}}{\text{EW}} \nabla\cdot\left(\omega^{1.5} D_{\text{nmw}} \nabla\lambda_{\text{nf}}\right) + S_{\text{nmw}} \tag{19}$$

where the source term considering the water production from the electrochemical reactions, electro-osmotic drag (EOD) effect and phase changes is

$$S_{\text{nmw}} = \begin{cases} -S_{\text{n-f}} \quad (\text{in membrane}) \\ \dfrac{j_{\text{c}}}{2F} - S_{\text{n-v}} - S_{\text{n-i}} + S_{\text{EOD}} \quad (\text{in cathode CL}) \\ -S_{\text{n-v}} - S_{\text{n-i}} + S_{\text{EOD}} \quad (\text{in anode CL}) \end{cases} \tag{20}$$

Mass conservation of frozen membrane water:

$$\frac{\rho_{\text{mem}}}{\text{EW}} \frac{\partial\left(\omega\lambda_{\text{f}}\right)}{\partial t} = S_{\text{fmw}} \tag{21}$$

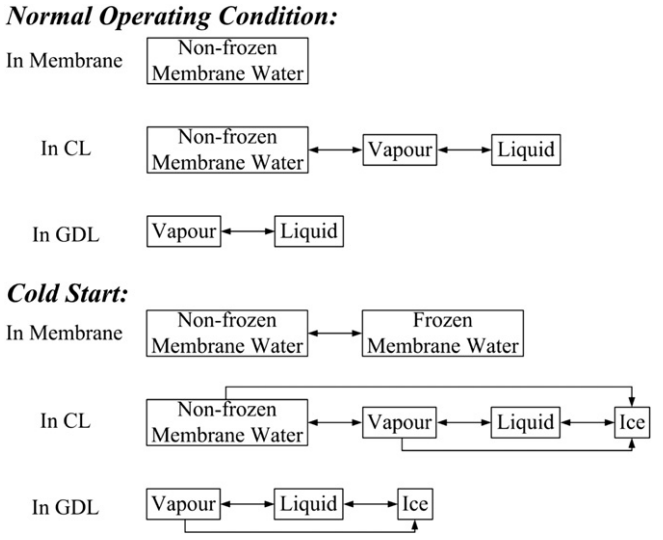

Fig. 2. Schematic diagram of water phase change and transport in various components of PEMFC in normal and cold start operating conditions [24].

$$a = \frac{X_{\text{vp}} p_{\text{g}}}{p_{\text{sat}}} + 2s_{\text{lq}} \tag{27}$$

$$\lambda_{\text{sat}} \begin{cases} = 4.837 \quad (\text{if } T < 223.15\ \text{K}) \\ = \left[-1.304 + 0.01479T - 3.594 \times 10^{-5} T^2\right]^{-1} \quad (\text{if } 223.15\ \text{K} \leq T < T_{\text{N}}) \\ > \lambda_{\text{nf}} \quad (\text{if } T \geq T_{\text{N}}) \end{cases} \tag{28}$$

$$S_{\text{fmw}} = S_{\text{n-f}} \tag{22}$$

$$S_{\text{n-f}} = \begin{cases} \xi_{\text{n-f}} \dfrac{\rho_{\text{mem}}}{\text{EW}} \left(\lambda_{\text{nf}} - \lambda_{\text{sat}}\right) & \left(\text{if } \lambda_{\text{nf}} \geq \lambda_{\text{sat}}\right) \\ \xi_{\text{n-f}} \dfrac{\rho_{\text{mem}}}{\text{EW}} \lambda_{\text{f}} & \left(\text{if } \lambda_{\text{nf}} < \lambda_{\text{sat}}\right) \end{cases} \tag{23}$$

$$S_{\text{EOD}} = \nabla\cdot\left(\frac{n_{\text{d}}}{F} \kappa_{\text{ion}}^{\text{eff}} \nabla\phi_{\text{ion}}\right) \tag{24}$$

In membrane, the phase change between frozen and non-frozen water is considered (Equation (23)). S_{EOD} (kmol m^{-3} s^{-1}) represents the water transport due to the electro-osmotic drag effect. The schematic of the water phase change considered in this model is also shown in Fig. 2 [24].

With the membrane hydration/dehydration considered in Equations (8) and (18), the non-frozen and frozen water contents ($\lambda_{\text{nf.f}}$), equilibrium water content (λ_{equil}), water activity (a) and saturation water content (λ_{sat}) are defined as

$$\lambda_{\text{nf.f}} = \frac{\text{EW}}{\rho_{\text{mem}}} c_{\text{nf,f}} \tag{25}$$

$$\lambda_{\text{equil}} = \begin{cases} 0.043 + 17.81a - 39.85a^2 + 36.0a^3 & (\text{if } 0 \leq a \leq 1) \\ 14.0 + 1.4(a-1) & (\text{if } 1 < a \leq 3) \end{cases} \tag{26}$$

The ionic conductivity is therefore a function of non-frozen water content rather than the total water content (the effect of water freezing on membrane conductivity is therefore considered):

$$\kappa_{\text{ion}} = \left(0.5139\lambda_{\text{nf}} - 0.326\right) \exp\left[1268\left(\frac{1}{303.15} - \frac{1}{T}\right)\right] \tag{29}$$

Electron transport:

$$0 = \nabla\cdot\left(\kappa_{\text{ele}}^{\text{eff}} \nabla\phi_{\text{ele}}\right) + S_{\text{ele}} \tag{30}$$

Ion transport:

$$0 = \nabla\cdot\left(\kappa_{\text{ion}}^{\text{eff}} \nabla\phi_{\text{ion}}\right) + S_{\text{ion}} \tag{31}$$

The source terms in the above two equations depend on the reaction rate in anode and cathode CLs:

$$S_{\text{ele}} = \begin{cases} -j_{\text{a}} \quad (\text{in anode CL}) \\ j_{\text{c}} \quad (\text{in cathode CL}) \\ 0 \quad (\text{in other zones}) \end{cases} \tag{32}$$

$$S_{\text{ion}} = \begin{cases} j_{\text{a}} \quad (\text{in anode CL}) \\ -j_{\text{c}} \quad (\text{in cathode CL}) \\ 0 \quad (\text{in other zones}) \end{cases} \tag{33}$$

where the reaction rates are defined as

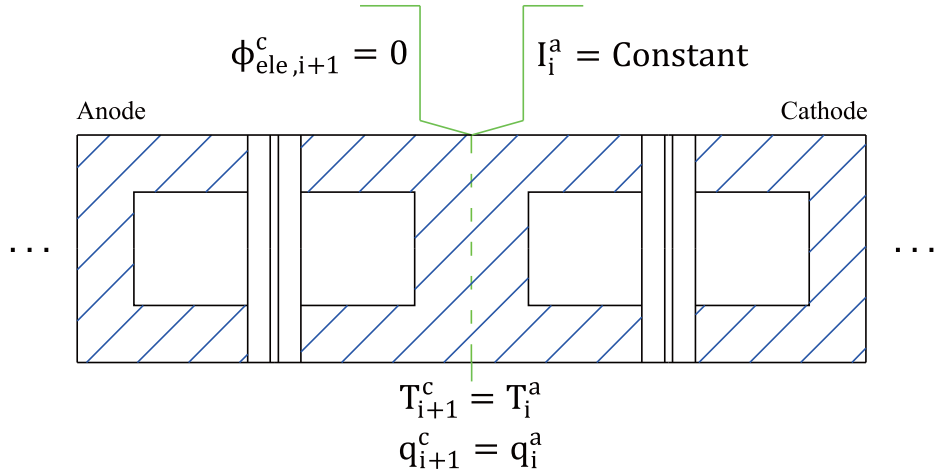

Fig. 3. Schematic diagram of the electrical and thermal boundary condition at the interface between single cells (two individual cells in a stack are shown as an example).

$$j_a = \left(1 - s_{lq} - s_{ice}\right) j^{ref}_{0,a} \left(\frac{c_{H_2}}{c^{ref}_{H_2}}\right)^{0.5} \times \left[\exp\left(\frac{2\alpha_a F}{RT}\eta_{act}\right) - \exp\left(-\frac{2\alpha_c F}{RT}\eta_{act}\right)\right] \quad (34)$$

$$j_c = \left(1 - s_{lq} - s_{ice}\right) j^{ref}_{0,c} \frac{c_{O_2}}{c^{ref}_{O_2}} \times \left[-\exp\left(\frac{4\alpha_a F}{RT}\eta_{act}\right) + \exp\left(-\frac{4\alpha_c F}{RT}\eta_{act}\right)\right] \quad (35)$$

A linear relationship between the ice formation and reaction rate is considered [24], therefore, if the CL is fully blocked by ice, the electrochemical reaction is stopped (the cold start process is failed).

Energy conservation equation:

$$\frac{\partial}{\partial t}\left((\rho C_p)^{eff}_{fl,sl} T\right) + \nabla\cdot\left((\rho C_p)^{eff}_{fl} \vec{u}_g T\right) = \nabla\cdot\left(k^{eff}_{fl,sl}\nabla T\right) + S_T \quad (36)$$

where the last term, S_T (W m^{-3}), is the source term:

$$S_T = \begin{cases} j_a|\eta_{act}| + \|\nabla\phi_{ele}\|^2\kappa^{eff}_{ele} + \|\nabla\phi_{ion}\|^2\kappa^{eff}_{ion} + S_{pc} \quad \text{(in anode CL)} \\ -\dfrac{j_c T\Delta S}{2F} + j_c|\eta_{act}| + \|\nabla\phi_{ele}\|^2\kappa^{eff}_{ele} + \|\nabla\phi_{ion}\|^2\kappa^{eff}_{ion} + S_{pc} \quad \text{(in cathode CL)} \\ \|\nabla\phi_{ele}\|^2\kappa^{eff}_{ele} + S_{pc} \quad \text{(in GDL)} \\ \|\nabla\phi_{ele}\|^2\kappa^{eff}_{ele} \quad \text{(in BP)} \\ \|\nabla\phi_{ion}\|^2\kappa^{eff}_{ion} + S_{pc} \quad \text{(in membrane)} \\ 0 \quad \text{(in other zones)} \end{cases} \quad (37)$$

where the latent heat, S_{pc} (W m^{-3}), is defined as

$$S_{pc} = \begin{cases} h_{cond}S_{v\text{-}l} + (h_{cond} + h_{fusn})S_{v\text{-}i} + h_{fusn}S_{l\text{-}i} \quad \text{(in GDL)} \\ h_{cond}\left(S_{v\text{-}l} - S_{n\text{-}v}M_{H_2O}\right) + (h_{cond} + h_{fusn})S_{v\text{-}i} + h_{fusn}\left(S_{l\text{-}i} + S_{n\text{-}i}M_{H_2O}\right) \quad \text{(in CL)} \\ h_{fusn}S_{n\text{-}f}M_{H_2O} \quad \text{(in membrane)} \\ 0 \quad \text{(in other zones)} \end{cases} \quad (38)$$

The heat generation includes the ohmic heat generated from the electric current though the stacks, activational heat generated from the electrochemical reaction, reversible heat due to the entropy change, and the latent heat due to the water phase change. The latent heat (Equation (38)) includes the corresponding heat generation and consumption caused by the water phase change considered in this study [30]. More details of the model formulation can also be found in Refs. [24,31].

2.4. Boundary and initial conditions

For single cell models, the voltage and/or current density are often set on the two end surfaces of the end plates (e.g. [31,32]). However, with more than one cells between the end plates, the electrical boundary condition is needed for each single cell.

Therefore, as shown in Fig. 3, internal electrical boundary condition is specified in the middle of each BP. Two virtual surfaces are assumed existing at the middle of each BP, and the two surfaces belong to the separated cells (one for the end of the anode of one cell, and another for the end of the cathode of the next cell).

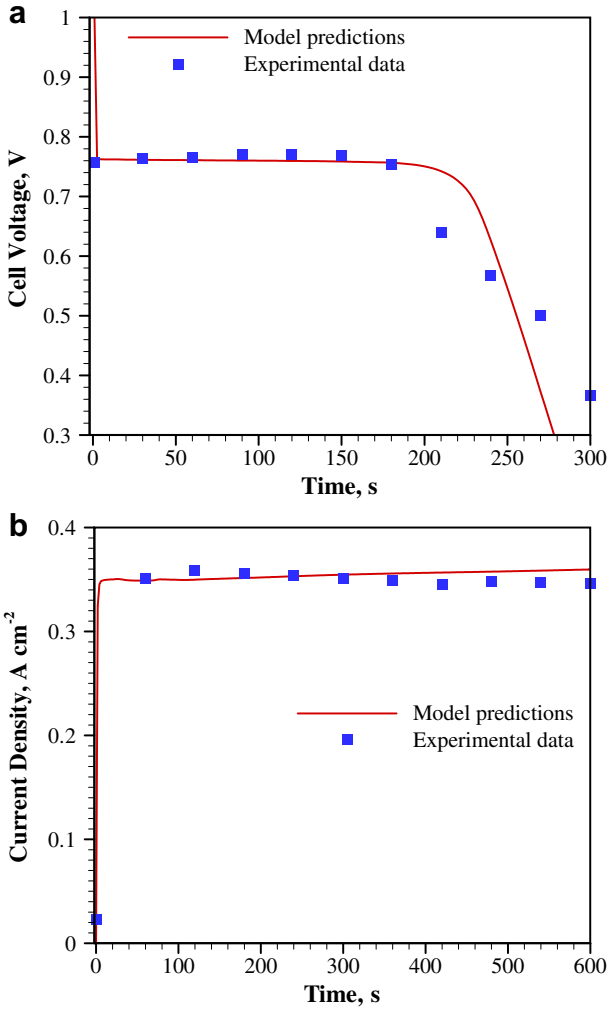

Fig. 4. Comparison between the model predictions and experimental data (a: from −10 °C at 0.07 A cm^{-2}; b: from −5 °C at 0.3 V) [37]. The stoichiometry ratio is 2.0, the initial water content is 6.2, the initial ice volume fraction is 0, and the inlet relative humidity is 0 [37].

Considering the fact that each single cell works at the same current density (connected in series), at the ends of the anodes of the single cells (on the virtual surfaces for anode and the anode end plate surface), the current density is defined to be the same for each cell to simulate the galvanostatic (constant current density) start-up condition:

$$I_1^{\mathrm{a}} = I_2^{\mathrm{a}} = \cdots = I_i^{\mathrm{a}} = \cdots = I_N^{\mathrm{a}} = \text{Constant} \tag{39}$$

where I (A cm^{-2}) is the current density; the subscripts 1, 2 and i represent Cell 1, Cell 2 and Cell i (the ith cell) in a stack, respectively; N represents the total number of cells; and the superscript a represents anode. The electronic potential is defined at the ends of the cathodes of the single cells (on the virtual surfaces for cathode and the cathode end plate surface):

Table 2
Six simulation cases.

Case no.	Case 1	Case 2	Case 3	Case 4	Case 5	Case 6
Number of cells	1	1	2	2	3	3
Current density (A cm^{-2})	0.05	0.1	0.05	0.1	0.05	0.1

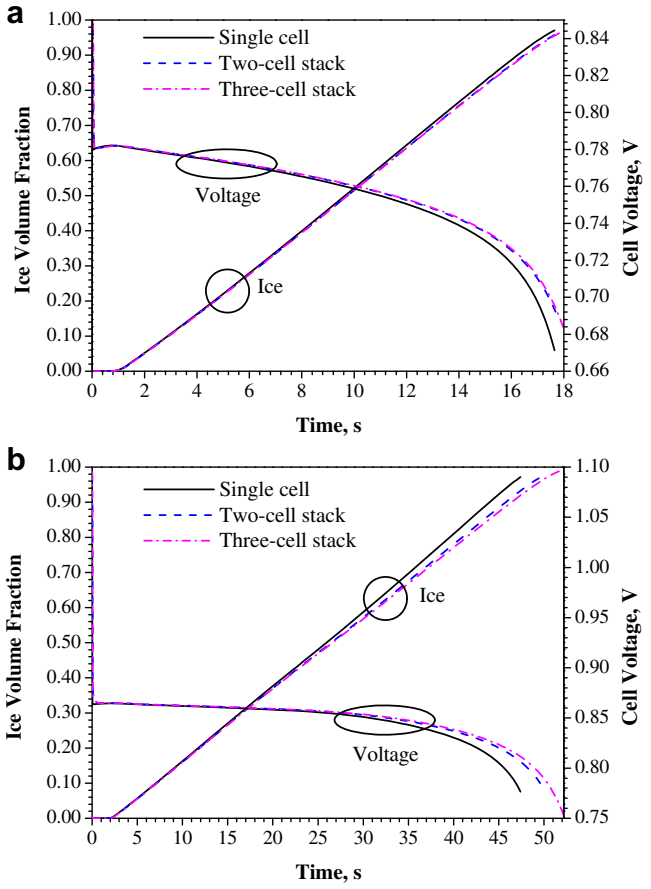

Fig. 5. Evolution of average voltages and volume averaged ice volume fraction in the cathode catalyst layers for single cell, two-cell stack and three-cell stack at the current densities of (a) 0.1 A cm^{-2} and (b) 0.05 A cm^{-2}. The initial, ambient and inlet gas temperatures are all −20 °C, the initial water content is 5, and the initial ice volume fraction is 0.

$$\phi_{\mathrm{ele},1}^{\mathrm{c}} = \phi_{\mathrm{ele},2}^{\mathrm{c}} = \cdots = \phi_{\mathrm{ele},i}^{\mathrm{c}} = \cdots = \phi_{\mathrm{ele},N}^{\mathrm{c}} = 0 \tag{40}$$

where ϕ (V) represents the electrical potential, and the subscript ele represents electrons. This boundary condition was also used in a previous stack model [33]. The assumption in this kind of

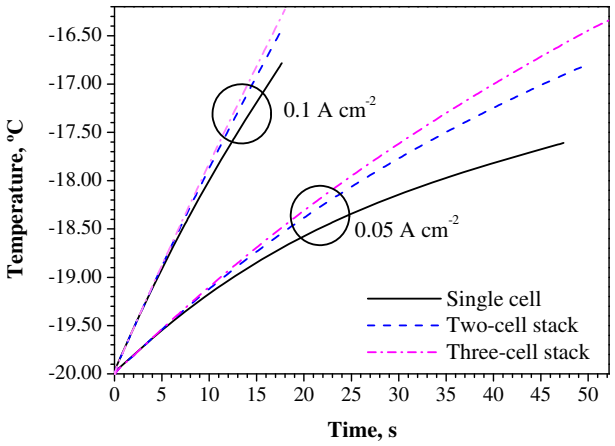

Fig. 6. Evolution of volume averaged stack and single cell temperatures for different current densities (0.1 A cm^{-2} and 0.05 A cm^{-2}) and numbers of cell (one cell, two cells and three cells). The initial, ambient and inlet gas temperatures are all −20 °C, the initial water content is 5, and the initial ice volume fraction is 0.

boundary condition is that the current density and voltage are evenly distributed at the interfaces between the individual cells. In this study, the active reaction area is only 1 cm^2 (single straight flow channel), much smaller than the commercial PEMFC stacks on the level of hundreds cm^2 [34,35], and the variation in 1 cm^2 was found to be insignificant [35]. Therefore, it is reasonable to assume that the current density and voltage are evenly distributed at the interfaces.

There should be no heat source or contact heat transfer resistance between the pairs of virtual surfaces defined above, therefore, for each pair of virtual surfaces, the internal thermal boundary condition is defined as

$$T_i^{a} = T_{i+1}^{c} \tag{41}$$

$$q_i^{a} = q_{i+1}^{c} \tag{42}$$

where T (K) stands for temperature, the equal temperature represents that there is no contact heat transfer resistance; and q (W m^{-2}) is the heat flux, representing the energy conservation between the two virtual surfaces.

The inlet boundary conditions of the flow channels are specified the same for each inlet port of the single cell in a stack, based on the common requirement of uniform reactant supply [36]. The mass

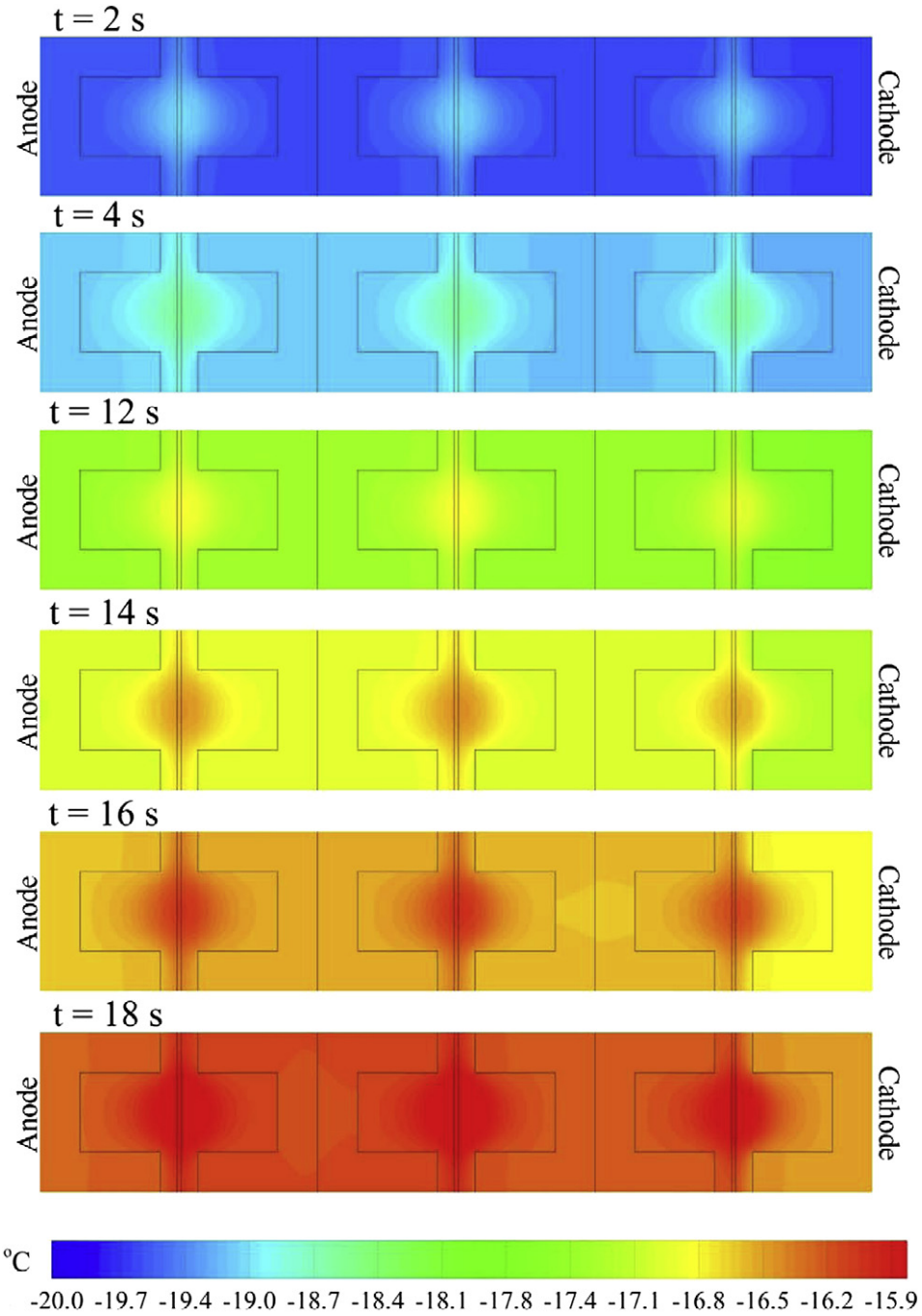

Fig. 7. Transient temperature distribution in the middle cross section in x–y planes (25 mm from the inlets) of the three-cell stack at 0.1 A cm^{-2}. The initial, ambient and inlet gas temperatures are all −20 °C, the initial water content is 5, and the initial ice volume fraction is 0.

flow rates at the inlets are defined as a function of several parameters:

$$\dot{m}_a = \frac{\rho_g^a \xi_a I_{ref} A}{2Fc_{H_2}}, \quad \dot{m}_c = \frac{\rho_g^c \xi_c I_{ref} A}{4Fc_{O_2}} \tag{43}$$

where I_{ref} (A cm^{-2}) is the reference current density; ρ_g^a (kg m^{-3}) and ρ_g^c (kg m^{-3}) are the densities of the gas mixtures supplied to flow channels; A (m^2) is the flat area of reaction surface; and c (kmol m^{-3}) represents the reactant concentration. The inlet gas temperature is set to be equal to the ambient temperature of −20 °C, the stoichiometric ratio is 2.0, and the inlet relative humidity is 0.

The sidewalls in this straight channel stack model are the middle surfaces between the parallel flow channels, on these walls the surface condition is set to be adiabatic due to the insignificant temperature difference between the neighboring channels as presented in the previous experimental work [14]. On the end walls of the end plates (as shown in Fig. 1), a heat transfer coefficient and the surrounding temperature are used to define thermal boundary condition:

$$\dot{Q} = hA_{wall}(T_{surr} - T_{wall}) \tag{44}$$

where $\dot{Q}$ (W) represents the heat transfer rate between the end walls of the stack and the ambient; h (W m^{-2} K^{-1}) is the heat transfer coefficient; A_{wall} (m^2) represents the surface area of the end wall; T_{surr} (K) is the surrounding/ambient temperature; and T_{wall} (K) is the surface temperature of the end wall of the stack.

For the initial conditions, the initial ice volume fraction is set to be 0, representing an effective purging process before the next cold start cycle; an initial water content of 5.0 is specified in the membranes and CLs; and the initial stack temperature is set to be −20 °C, which equals to the ambient temperature.

2.5. Numerical procedures

This PEMFC stack cold start model is implemented with the user-defined function (UDF) of the computational fluid dynamics (CFD) program FLUENT. Finite volume method is adopted to discretize and solve the conservation equations. Grid independent study has been carried out to ensure the rationality of the simulations, and the whole computational domain has 228,000 cells for the three-cell stack shown in Fig. 1. The second-order upwind discretization method is used. The pressure-implicit with splitting of operators (PISO) algorithm is adopted which is based on the higher degree of the approximate relation between the corrections for pressure and velocity, and it is effective in decreasing the iteration times required for convergence when solving a transient problem. The convergence is accelerated by an algebraic multigrid (AMG) method with the Gauss–Seidel smoother. The minimum and maximum time step sizes are 0.005 s and 0.1 s for the simulations. Convergence criteria with a residual of 10^{-8} are used for all the variables.

3. Results and discussion

This model has been comprehensively compared with experimental results with reasonable agreements [37]. As shown in Fig. 4, both the failed (from −10 °C at 0.07 A cm^{-2}) and successful (from −5 °C at 0.3 V) cold start processes are compared, and the operating conditions in the numerical simulations are defined corresponding to the experiments [37]. The stoichiometry ratio is 2.0, the initial water content is 6.2, the initial ice volume fraction is 0 in all components, and the inlet relative humidity is 0.

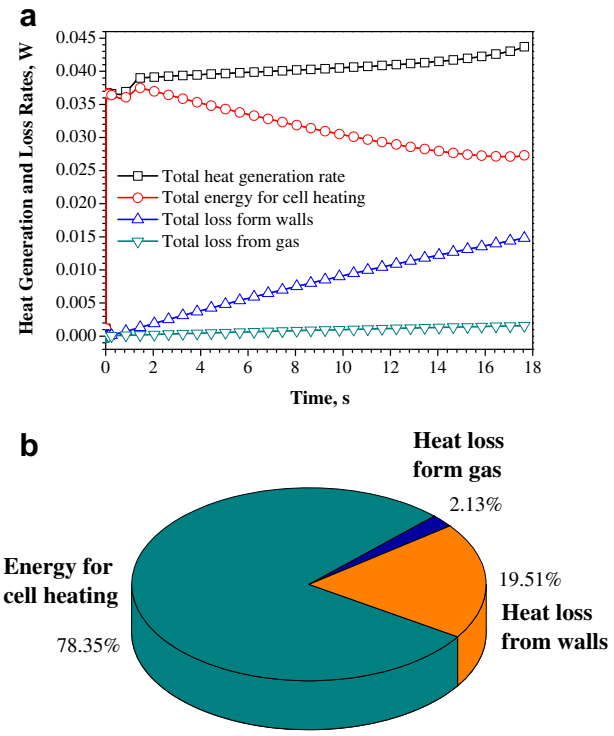

Fig. 8. Various heat generation and loss rates during the cold start process of the single cell at 0.1 A cm^{-2}; (a) transient variation; (b) percentage distribution for the complete cold start process. The initial, ambient and inlet gas temperatures are all −20 °C, the initial water content is 5, and the initial ice volume fraction is 0.

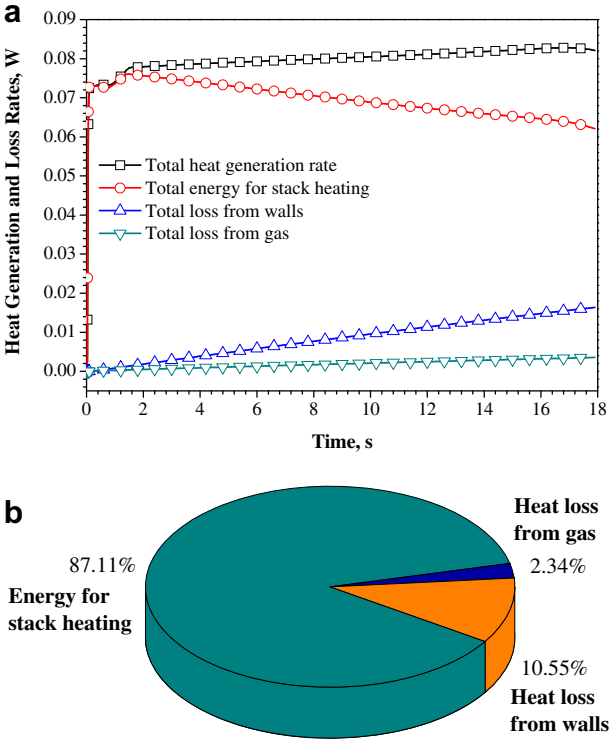

Fig. 9. Various heat generation and loss rates during the cold start process of the two-cell stack at 0.1 A cm^{-2}; (a) transient variation; (b) percentage distribution for the complete cold start process. The initial, ambient and inlet gas temperatures are all −20 °C, the initial water content is 5, and the initial ice volume fraction is 0.

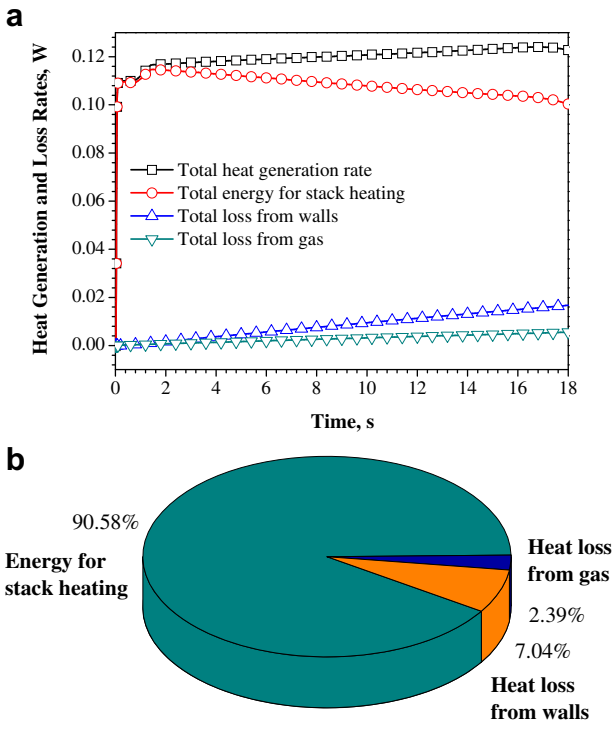

Fig. 10. Various heat generation and loss rates during the cold start process of the three-cell stack at 0.1 A cm^{-2}; (a) transient variation; (b) percentage distribution for the complete cold start process. The initial, ambient and inlet gas temperatures are all −20 °C, the initial water content is 5, and the initial ice volume fraction is 0.

The results of this study are discussed in four parts: the first part compares the single cell and the stacks with different numbers of cells; the second part compares the different cells in the three-cell stack; the third part compares the single cell to the middle cell inside the three-cell stack; and the last part presents the effect of current density. The results for the effect of cell numbers on start-up time in Ref. [26] showed that the start-up time changes from single cell to stack, and when the cell number reaches three, the performance becomes similar with more cell numbers. Therefore, only single cell, two-cell stack and three-cell stack are considered in this study to save the computational time, and the computational domain for the three-cell stack with straight flow channels is shown in Fig. 1. Six cases are considered in this study as listed in Table 2. All the simulations are stopped when the volume averaged ice volume fraction in cathode CL approaches 1, because this is the indication of a completely failed cold start process. Galvanostatic (constant current density) start-up mode is adopted for all the cases; the number of cells varies from one to three; and two different current densities of 0.05 A cm^{-2} and 0.1 A cm^{-2} are considered. Detailed design and operating parameters are given in Table 1.

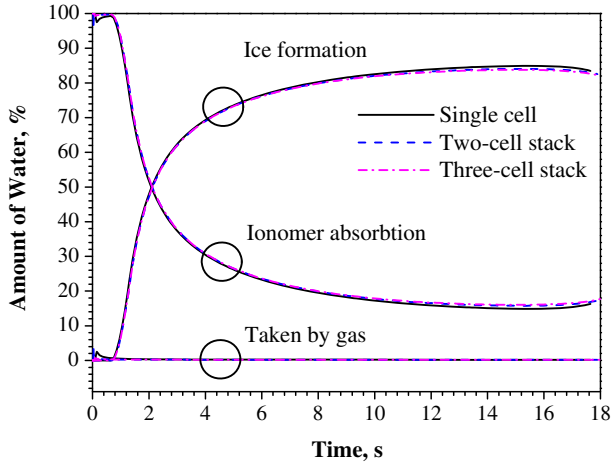

Fig. 11. Water content of diverse states in different stacks and single cell at 0.1 A cm^{-2}. The initial, ambient and inlet gas temperatures are all −20 °C, the initial water content is 5, and the initial ice volume fraction is 0.

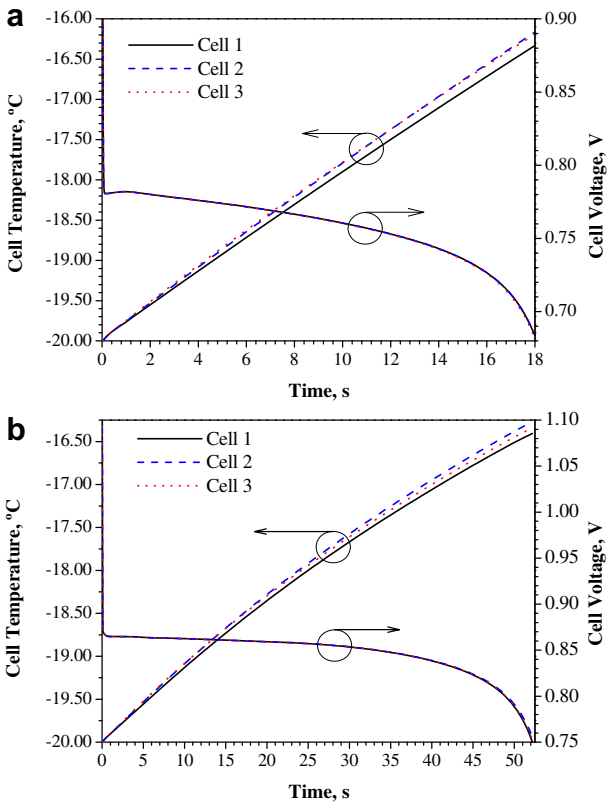

Fig. 12. Evolution of volume averaged cell temperatures and voltages of the individual cells in the three-cell stack at the current densities of (a) 0.1 A cm^{-2} and (b) 0.05 A cm^{-2}. The initial, ambient and inlet gas temperatures are all −20 °C, the initial water content is 5, and the initial ice volume fraction is 0.

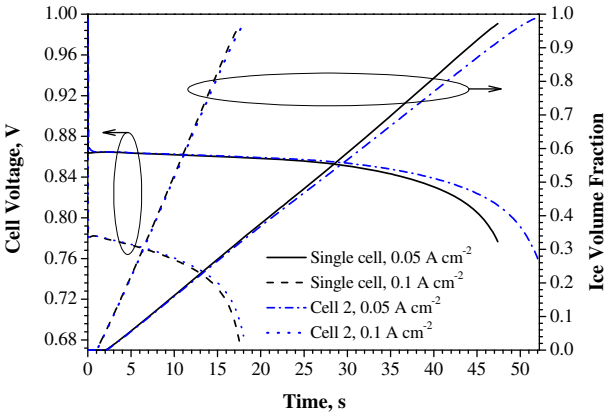

Fig. 13. Evolution of cell voltages and volume averaged ice volume fractions in cathode catalyst layers for the single cell and Cell 2 of the three-cell stack at different current densities. The initial, ambient and inlet gas temperatures are all −20 °C, the initial water content is 5, and the initial ice volume fraction is 0.

3.1. Comparison of single cell and stacks

Fig. 5 shows the comparison of the average voltage of each cell and volume averaged ice volume fraction in the cathode CLs in the stacks and the single cell. It can be noticed that the cell voltages are almost the same for the stacks and single cell at the beginning, as the ice in the CLs accumulates, the voltage decreases gradually, and the difference among the stacks and single cell becomes more and more notable. Furthermore, the voltage decreases more slowly if the stack has more cells. The evolution of the ice volume fraction is also similar among the different stacks and single cell, and as the number of cells increases, the ice volume fraction increases more slowly. At the lower current density of 0.05 A cm^{-2}, since the ice formation rate is lower than that at the higher current density of 0.1 A cm^{-2}, the difference in start-up time is more significant.

The difference in the voltages and ice formation rates are related to the different temperature evolution, as shown in Fig. 6. It shows that the volume averaged temperature increases faster for the stacks with more cells, which can reach higher temperature at the end of the cold start processes. It can also be noticed that a higher

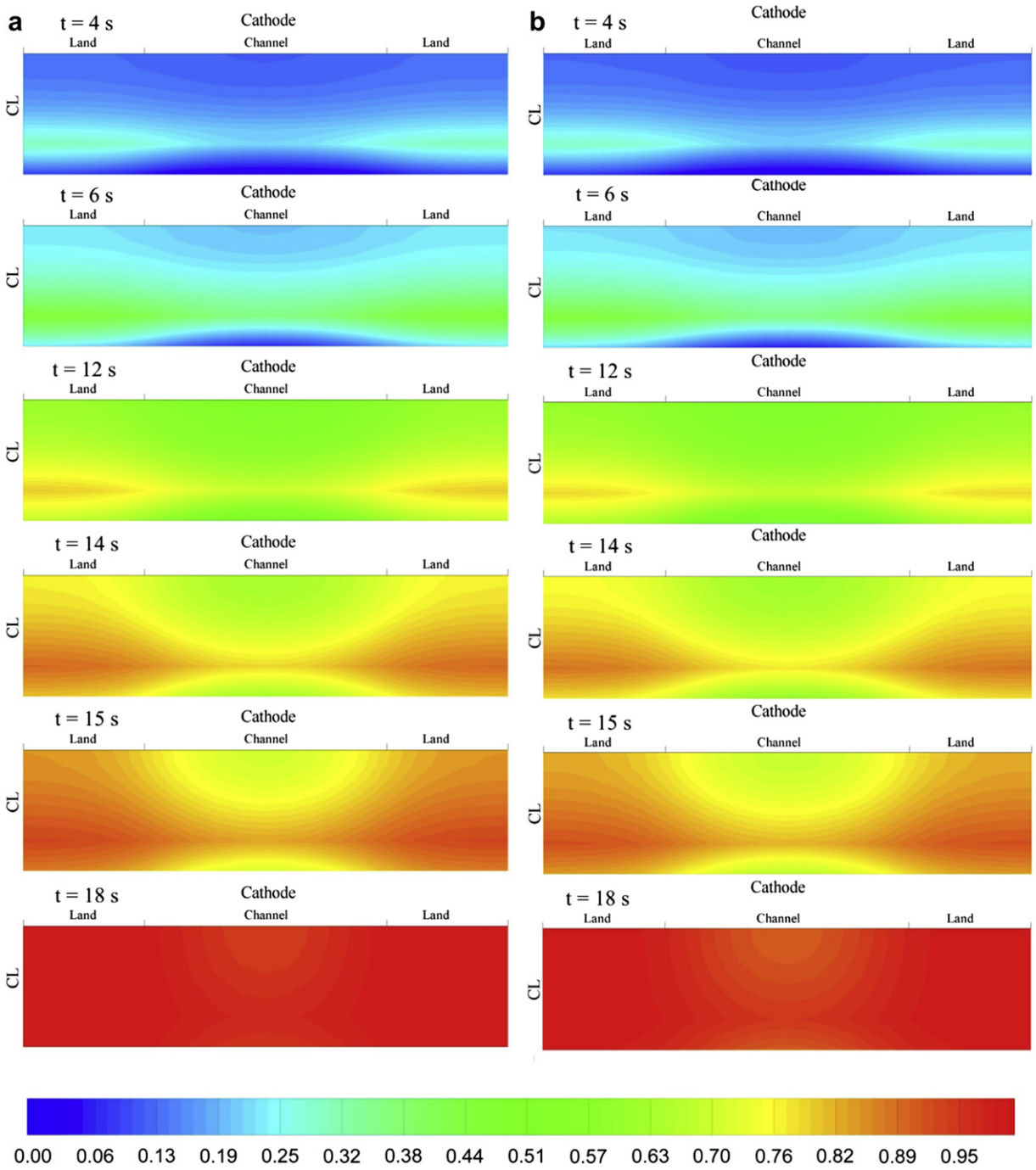

Fig. 14. Distribution of ice volume fraction during the start-up processes in the cathode catalyst layers in x–y planes in the center of the stack (25 mm from the inlets) at a current density of 0.1 A cm^{-2}; (a) the cathode catalyst layer of the single cell; (b) the cathode catalyst layer of Cell 2 in the three-cell stack. The initial, ambient and inlet gas temperatures are all −20 °C, the initial water content is 5, and the initial ice volume fraction is 0.

current density is favorable for increasing the temperature. At the current density of 0.1 A cm^{-2}, the single cell can reach the temperature of −16.8 °C, while the two-cell stack reaches −16.5 °C, and the three-cell stack sustained a bit longer which reaches −16.2 °C. With a lower current density, the temperature difference between different stacks and single cell is larger due to the longer start-up processes. The cell voltage depends on the reversible voltage and overpotential, and the reversible voltage decreases as the temperature increases, while the overpotential is lower at higher temperature and higher with more ice (less reaction area). Obviously, the overpotential plays the major role in this case. In addition, the ice formation rate is lower at higher temperature because the ionomer can absorb more product water.

The transient temperature distribution of the three-cell stack is shown in Fig. 7. The temperature distribution of the single cell and two-cell stack in the same cross section is not shown here, the single cell condition can be found in the previous work [24], and the two-cell stack condition is similar to the three-cell stack. During a cold start process, the temperature is mainly influenced by four different kinds of heating sources as previously mentioned. As shown in Fig. 7, for each individual cell in the stack, the temperature increases through the cell from the MEA to the BPs, because the main heat sources are the ohmic heat from the membranes and CLs as well as the activational heat from the cathode CLs. The temperature of the cell in the middle is higher than those outside because the middle cell is further away from the end plate surfaces which dissipate heat to the surroundings. The temperature of the cathode end plate is lower than the anode, because more ohmic heat is generated on the anode side. The ohmic heat is higher on the anode side because the ionomer close to the anode is dryer than the cathode due to the electro-osmotic drag effect, resulting in higher ohmic resistance of the ionomer close to the anode.

To further explain the temperature distribution in Fig. 7, the evolution of various heat generation and loss rates for the single cell and stacks is shown in Figs. 8–10. Fig. 8(a) shows the transient variation of the total heat generation rate and heat loss rates through different ways for the single cell, and Fig. 8(b) shows the corresponding percentages of total heat generation and losses for the complete cold start process (0–18 s); and the corresponding results for the two-cell stack and three-cell stack are shown in Figs. 9 and 10. In Figs. 8(a), 9(a) and 10(a), the total heat generation rate is the sum of the four heat sources including the ohmic heat, activational heat, reversible heat and latent heat. For the single cell and stacks, the total heat generation rate increases slightly during the cold start process as a combined effect of the dryness of the anode CL and an increase of overpotential. As three ways of heat transfer are considered which include the heat absorbed by PEMFC, loss from walls (end plate surfaces) and loss from reactant gases. The tendencies of transient variation for the heat transfer are also similar among the single cell and stacks. As shown in Fig. 8(a), the proportion of heat which dissipates to environment increases during the start-up process, correspondingly, the proportion of heat to raise the cell temperature decreases. The increment of heat loss rate is a result of the increased cell temperature. Moreover, due to the low heat capacity of hydrogen and air comparing with the solid materials, the heat loss from the gases is insignificant. By comparing the different stacks and single cell, it can be found that the total heat generation rate increases almost proportionally with the cell numbers, and together with the fact that the increased rates of heat loss from the walls are almost the same, the proportion of heat loss from the walls decreases as the cell number increases while the proportion of heat absorbed by PEMFC increases, as shown in Figs. 8(b), 9(b) and 10(b). With the number of cells increases from one to three, the proportion of heat loss from walls for the whole start-up process decreases from 19.51% to 7.04%, and the proportion of heat absorbed by PEMFC increases from 78.35% to 90.58%. The results indicate that increasing the number of cells of stacks improves the cold start performance.

The water generation, phase change and transport are important factors affecting the cold start performance. The formed water freezes to ice during a cold start process once the ionomer is saturated. Fig. 11 shows the water content evolution in diverse states (ice formation, ionomer absorption and evaporation) of different stacks and single cell. The total water generation rate is the same for the individual cells of different stacks and single cell in the galvanostatic mode. Therefore, the ice formation, ionomer absorption and evaporation share the constant water generation. Among them, the water evaporation (taken away by gas) is insignificant as shown, due to the low saturation pressure of water vapor at subzero temperatures. The discrepancies between the different stacks and single cell are subtle. The ionomer in the stacks with more cells can absorb more water, due to the higher saturation water content at the higher temperature. Fig. 11 explains the lower ice formation rate of the stacks with more cells, and as the number of cells further increases, it is suggested that this effect might be more notable.

3.2. Comparison of different cells in three-cell stack

For the three-cell stack, the individual cells are defined as Cell 1, Cell 2 and Cell 3, representing the cell on the cathode side, in the middle and on the anode side, respectively, as demonstrated in Fig. 1. The evolution of volume averaged cell temperatures and voltages of the individual cells in the three-cell stack at different current densities is shown in Fig. 12. It can be noticed that no apparent difference exists among the voltages of the different individual cells, the uniform reactants supply is one of the reasons of this result. The evolution of temperature for different cells is similar with each other, with slight discrepancy that the temperature of Cell 2 is the highest as it is far from the end surfaces. The temperature of Cell 3 is higher than Cell 1 because the heat source is larger on the anode side for each cell.

3.3. Comparison of the single cell and the middle cell (Cell 2) of three-cell stack

Since Cell 2 (better heat insulation, with other cells on its both sides) of the three-cell stack is similar to the individual cells

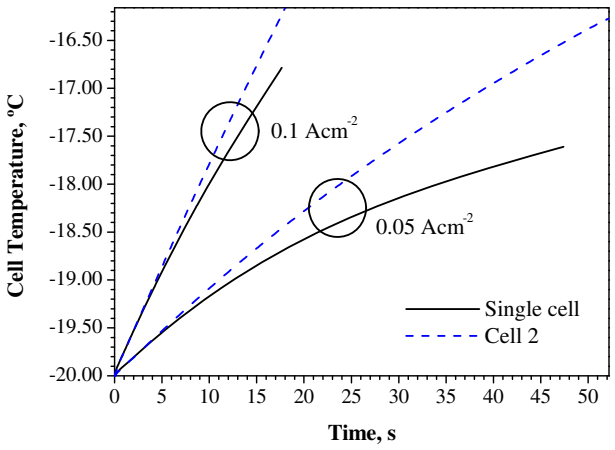

Fig. 15. Evolution of volume averaged cell temperature of the single cell and Cell 2 of the three-cell stack at different current densities. The initial, ambient and inlet gas temperatures are all −20 °C, the initial water content is 5, and the initial ice volume fraction is 0.

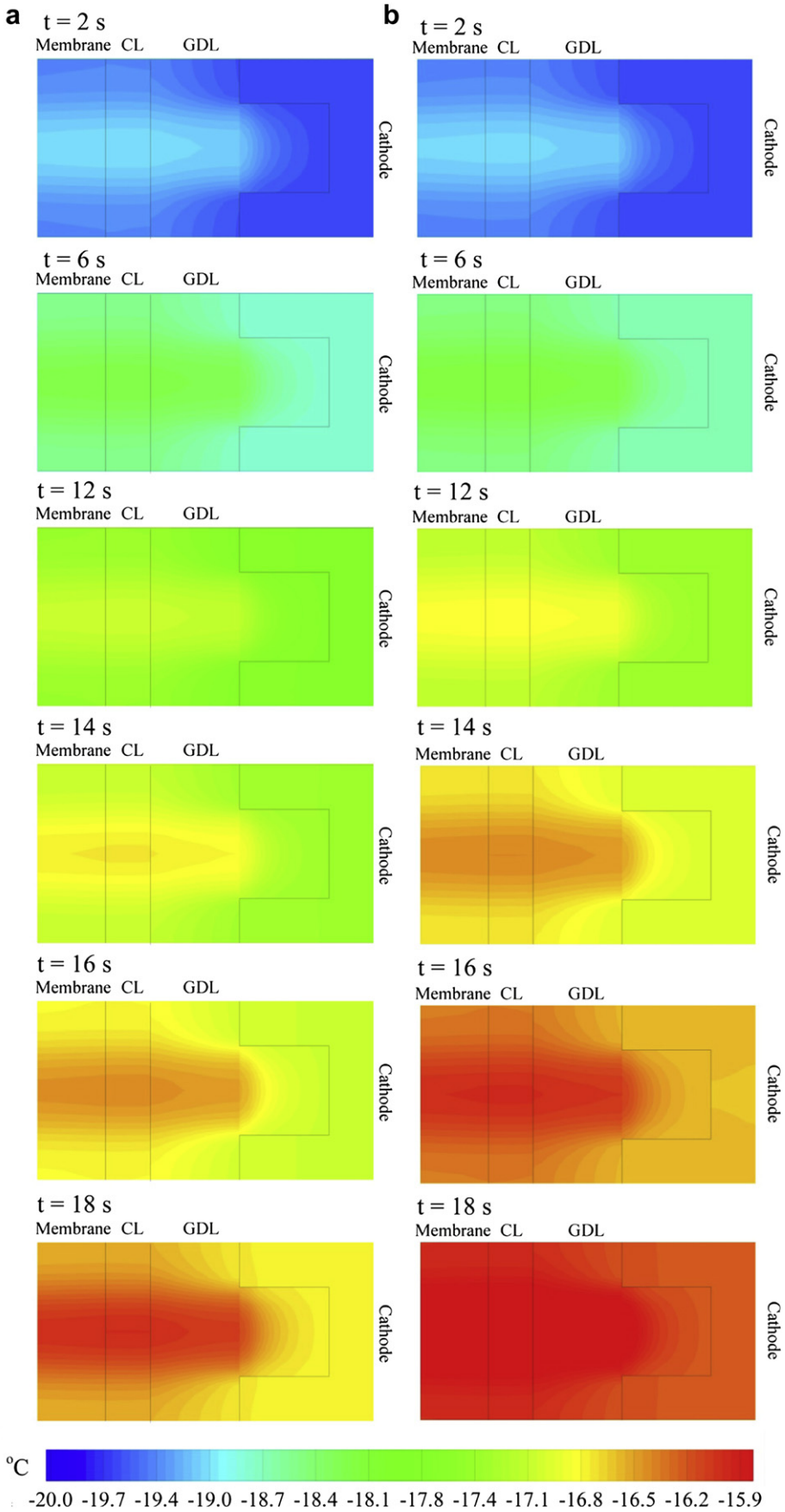

Fig. 16. Transient temperature distribution in partial components of the single cell and Cell 2 of the three-cell stack in x–y plane in the center of the cells (25 mm form the inlets) at a current density of 0.1 A cm^{-2}; the components include the membrane, cathode catalyst layer, cathode gas diffusion layer, cathode flow channel and bi-polar plate, and the relative scales of each component shown are adjusted for clear recognization; (a) the components of the single cell; (b) the components of Cell 2 in the three-cell stack. The initial, ambient and inlet gas temperatures are all −20 °C, the initial water content is 5, and the initial ice volume fraction is 0.

between the two end cells of the stacks with more cells, the cold start performance of Cell 2 is representative for a large practical PEMFC stack with many individual cells. Therefore, comparing Cell 2 of the three-cell stack and the single cell helps understand the difference between practical stacks and single cell. Fig. 13 shows the evolution of cell voltages and ice volume fractions in the cathode CLs of the single cell and Cell 2 of the three-cell stack at different current densities. It can be noticed that the ice formation rate of the single cell is higher than that of Cell 2. The cell voltages drop slightly in the early period of the start-up processes, followed by the sharp decrements of voltage when the cathode CLs are almost full of ice, and notable difference in voltage evolution also appears near the end of the cold start processes. For the single cell, since the cathode CL is blocked by ice more quickly, the sharp voltage drop happens more quickly than Cell 2 of the three-cell stack.

Fig. 15 shows the ice volume fraction in the cathode CLs for the single cell and Cell 2 of the three-cell stack at the current density of 0.1 A cm^{-2}. Ice is first formed under the land and then under the flow channel, because the under land region has lower temperature. By comparing Fig. 14(a) and (b), it can be found that for the single cell, ice is formed faster than Cell 2 of the three-cell stack, especially in the direction from the inner region of the cathode CL to BP. This phenomenon is mainly caused by the different temperatures.

Fig. 15 shows the evolution of volume averaged cell temperature of the single cell and Cell 2 of the three-cell stack at different current densities. It can be noticed that the average temperature of Cell 2 increases faster than that of the single cell, because Cell 2 is thermally insulated by the outside cells while the single cell is exposed to ambient directly. More detailed feature of temperature distribution can be found in Fig. 16. This figure shows part of the single cell and Cell 2, which include the membrane, cathode CL, cathode GDL, cathode flow channel and BP, the scale of each component is adjusted for clear recognition. It can be noticed that the temperature distribution of Cell 2 is more uniform than the single cell. The BP of the single cell dissipates heat directly to the low temperature ambient, and because the thermal conductivity of BP is much higher than the other components, the temperature distribution in the BP is more uniform, and large temperature gradient exists in the MEA. Furthermore, with the high thermal conductivity of the BP, in the MEAs, the temperature is lower under the land. It can also be noticed that the temperature distribution in the MEA is more uniform in Cell 2 than the single cell, because the cooling effect of the BP on the MEA is weaker with Cell 2. It can also be noticed that the temperature variation is insignificant at the membrane/CL and CL/GDL interfaces, due to the similar thermal conductivities of these materials (Table 1); and the temperature variation is noticeable at the GDL/BP, GDL/channel and BP/channel interfaces, due to the different thermal conductivities of the materials and the relatively strong convective heat transfer in the flow channel.

The evolution and percentage distribution of heat generation and loss rates of the single cell and Cell 2 of the three-cell stack through various ways at 0.1 A cm^{-2} are shown in Fig. 17. Comparing Figs. 17(a) and 8(a) show that the heat loss rate keeps almost zero within the first 3 s for Cell 2, indicating that the surrounding does not impact the inside cells of stack in the first few seconds. The

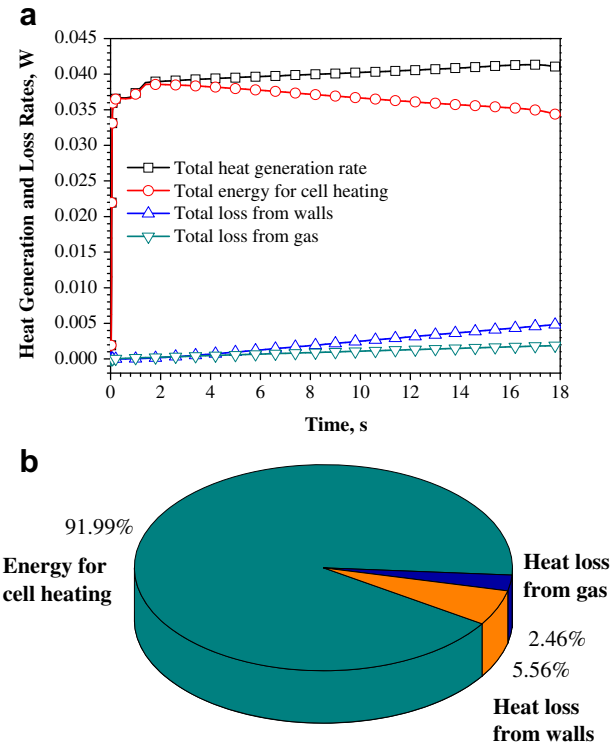

Fig. 17. Various heat generation and loss rates during the cold start process of Cell 2 of the three-cell stack at 0.1 A cm^{-2}; (a) transient variation; (b) percentage distribution for the complete cold start process. The initial, ambient and inlet gas temperatures are all −20 °C, the initial water content is 5, and the initial ice volume fraction is 0.

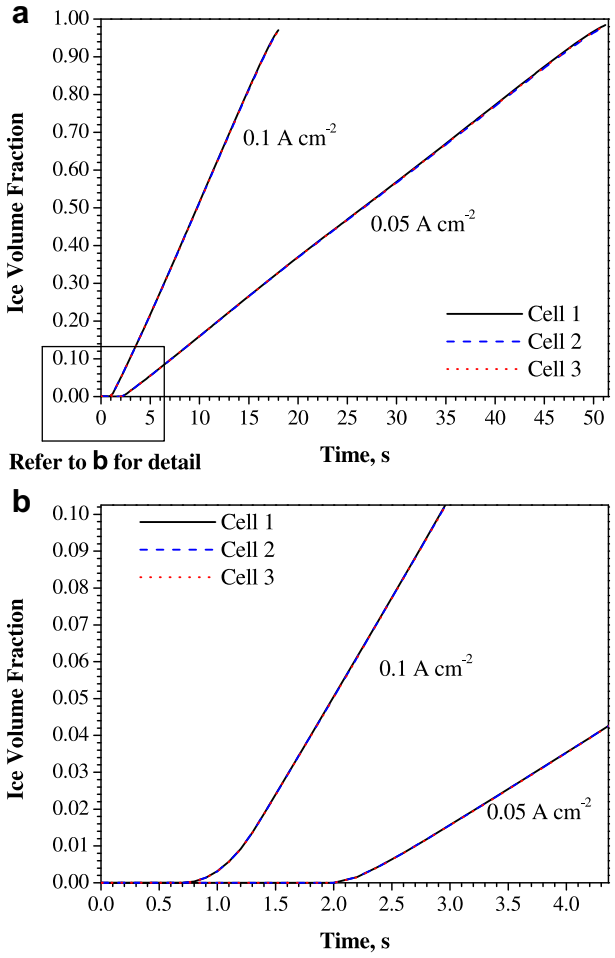

Fig. 18. Evolution of volume averaged ice volume fraction in the cathode catalyst layers of the individual cells in the three-cell stack at different current densities. The initial, ambient and inlet gas temperatures are all −20 °C, the initial water content is 5, and the initial ice volume fraction is 0.

increment of heat loss from walls (the virtual middle faces of BPs) of Cell 2 is much lower than that of the single cell due to the better thermal insulation of Cell 2. Fig. 17(b) shows the percentage distribution of various heat losses integrated though the whole starting process. The heat utilized to increase the temperature is 91.99% of the total heat generation, which is much higher than the value of the single cell of 76.67%. The better heat insulation of Cell 2 indicates that most of the cells in a large practical PEMFC stack have

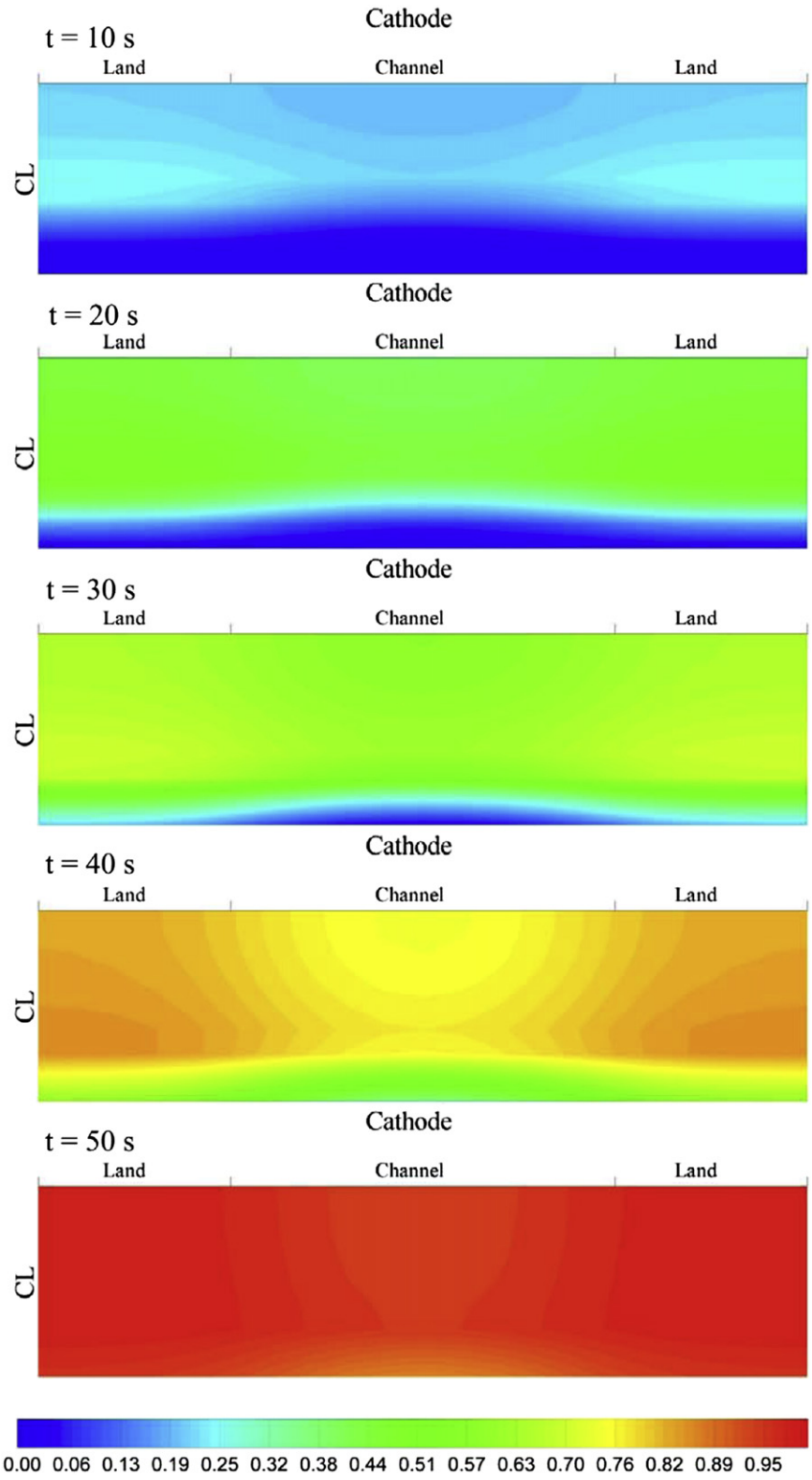

Fig. 19. Transient distribution of ice volume fraction during the start-up processes in the cathode catalyst layer of Cell 2 in x–y plane in the center of the stack (25 mm from the inlets) at the current density of 0.05 A cm^{-2}. The initial, ambient and inlet gas temperatures are all −20 °C, the initial water content is 5, and the initial ice volume fraction is 0.

better cold start performance than a single cell, while the cells located outside are similar to a single cell due to the direct heat loss to the ambient. Therefore, strategies to assist cold start should focus on the outside cells.

3.4. Effect of current density

Fig. 18 shows the evolution of volume averaged ice volume fraction in cathode CL of each cell of the three-cell stack at different current densities, and no noticeable difference can be found between the different cells at the same current density. However, the influence of current density is significant. A higher current density results in a higher ice formation rate, and as Fig. 18(b) shows, at the current density of 0.1 A cm^{-2}, ice starts to be formed at about 0.8 s, while at 0.05 A cm^{-2}, ice appears at around 2 s. The reason is that with a lower water generation rate (lower current density), the ionomer has more time to absorb the product water, on the other hand, at a higher current density, the ionomer in the cathode CL gets saturated more quickly.

Fig. 19 shows the transient ice volume fraction distribution in the cathode CL in Cell 2 of the three-cell stack at 0.05 A cm^{-2}, as a comparison, Fig. 14(b) shows the ice distribution at the same location while at a higher current density (0.1 A cm^{-2}). It can be found that in both cases the ice appears first under the land. However, at the lower current density, ice is formed faster at a section close to the BP side than the membrane side; on the other hand, at the higher current density, ice is formed at a section close to the membrane side. The different ice distributions at different current densities are caused by start-up duration. With a lower current density, the membrane water absorption effect is more significant due to the longer duration, therefore, more water at the sections close to the membrane can be absorbed by the membrane; on the other hand, such effect is less significant at a higher current density, and the sections close to the membrane side form ice first because of the higher reaction rate.

4. Conclusion

To understand the details of proton exchange membrane fuel cell (PEMFC) stack cold start processes, a three-dimensional multiphase stack model has been developed and numerical simulations have been conducted. It is found that notable voltage discrepancies between different stacks and single cell occur when the ice almost fully blocks the cathode catalyst layer (CL), and for the stacks with more cells, the voltage decreases more slowly due to the lower ice formation rate. The temperature increases faster for a stack with more cells, and a higher temperature can be reached at the end of the cold start process. No apparent difference in voltage exists among the different individual cells in a stack when the reactant gases are evenly supplied to each cell. The temperature of the individual cell in the middle of a stack is higher and more evenly distributed than those on the sides and single cells, due to weakened cooling effect of the bi-polar plate (BP) on the membrane electrode assembly (MEA), and the ice formation rate is also lower in the middle cell. The temperature of the individual cell in a stack on the anode side is higher than on the cathode side due to the higher ohmic heat in the anode. At a lower current density, the ice in the cathode CL is formed faster at the section close to the BP, and it is close to the membrane at a higher current density.

Acknowledgments

This research is supported by the National Natural Science Foundation of China (Grant No. 51276121), the National Basic Research Program of China (973 Program) (Grant No. 2012CB215500), and the Natural Science Foundation of Tianjin (China) (Grant No. 12JCYBJC30500).

References

[1] C. Spiegel, Designing and Building Fuel Cells, McGraw-Hill, New York, 2007.
[2] A.Z. Weber, J. Newman, C. Radke, Fuel Cell Fundamentals at Low and Subzero Temperatures (2011).http://www.hydrogen.energy.gov/annual_progress11_fuelcells.html (accessed 18.05.12).
[3] 2011 Annual Implementation Plan of Fuel Cells and Hydrogen Joint Undertaking (2011).http://www.fch-ju.eu/page/documents/ (accessed 18.05.12).
[4] H. Koguchi, Research and Development of Fuel Cells and Hydrogen in Japan (2010).http://www.fch-ju.eu/gapage/presentations-given-fch-ju-stakeholders-general-assembly-2010/ (accessed 18.05.12).
[5] G. Skala, Automotive PEM Stack Freeze Requirements & Suggested Fundamental Studies (2005).http://www1.eere.energy.gov/hydrogenandfuelcells/fc_freeze_workshop.html (accessed 18.05.12).
[6] S. Ge, C.Y. Wang, Electrochimica Acta 52 (2007) 4825–4835.
[7] J. Hou, B. Yi, H. Yu, L. Hao, W. Song, Y. Fu, Z. Shao, International Journal of Hydrogen Energy 32 (2007) 4503–4509.
[8] K. Tajiri, Y. Tabuchi, C.Y. Wang, Journal of the Electrochemical Society 154 (2007) B147–B152.
[9] E. Schießwohl, T. von Unwerth, F. Seyfried, D. Brüggemann, Journal of Power Sources 193 (2009) 107–115.
[10] Z. Miao, H. Yu, W. Song, L. Hao, Z. Shao, Q. Shen, J. Hou, B. Yi, International Journal of Hydrogen Energy 35 (2010) 5552–5557.
[11] M. Luo, C. Huang, W. Liu, Z. Luo, M. Pan, International Journal of Hydrogen Energy 35 (2010) 2986–2993.
[12] W. Song, H. Yu, L. Hao, B. Yi, Z. Shao, International Journal of Hydrogen Energy 35 (2010) 11129–11137.
[13] S.Y. Lee, H.J. Kim, E. Cho, K.S. Lee, T.H. Lim, I.C. Hwang, J.H. Jang, International Journal of Hydrogen Energy 35 (2010) 12888–12896.
[14] K. Jiao, I.E. Alaefour, G. Karimi, X. Li, Electrochimica Acta 56 (2011) 2967–2982.
[15] G. Gavello, J. Zeng, C. Francia, U.A. Icardi, A. Graizzaro, S. Specchia, International Journal of Hydrogen Energy 36 (2011) 8070–8081.
[16] M. Miller, A. Bazylak, Journal of Power Sources 196 (2011) 601–613.
[17] P. Oberholzer, P. Boillat, R. Siegrist, R. Perego, A. Kastner, E. Lehmann, G.G. Scherer, A. Wokaun, Journal of the Electrochemical Society 159 (2012) B235–B245.
[18] A. Santamaria, H.Y. Tang, J.W. Park, G.G. Park, Y.J. Sohn, International Journal of Hydrogen Energy (2012). http://dx.doi.org/10.1016/j.ijhydene.2012.04.093.
[19] Y. Wang, Journal of the Electrochemical Society 154 (2007) B1041–B1048.
[20] L. Mao, C.Y. Wang, Journal of the Electrochemical Society 154 (2007) B139–B146.
[21] Y. Wang, P.P. Mukherjee, J. Mishler, R. Mukundan, R.L. Borup, Electrochimica Acta 55 (2010) 2636–2644.
[22] L. Mao, C.Y. Wang, Y. Tabuchi, Journal of the Electrochemical Society 154 (2007) B341–B351.
[23] H. Meng, Journal of Power Sources 178 (2008) 141–150.
[24] K. Jiao, X. Li, Electrochimica Acta 54 (2009) 6876–6891.
[25] M. Sundaresan, R.M. Moore, Journal of Power Sources 145 (2005) 534–545.
[26] M. Khandelwal, S. Lee, M.M. Mench, Journal of Power Sources 172 (2007) 816–830.
[27] R.K. Ahluwalia, X. Wang, Journal of Power Sources 162 (2006) 502–512.
[28] H. Meng, B. Ruan, International Journal of Energy Research 35 (2011) 2–14.
[29] K. Jiao, X. Li, Progress in Energy and Combustion Science 37 (2011) 221–291.
[30] E.L. Thompson, T.W. Capehart, Timothy.J. Fuller, J. Jorne, Journal of the Electrochemical Society 154 (2006) A2351–A2363.
[31] K. Jiao, X. Li, International Journal of Hydrogen Energy 34 (2009) 8171–8184.
[32] K. Jiao, X. Li, International Journal of Hydrogen Energy 35 (2010) 5077–5094.
[33] Y.Y. Shan, S.Y. Choe, Journal of Power Sources 158 (2006) 274–286.
[34] http://www.ballard.com/fuel-cell-products/fc-velocity-9ssl.aspx.
[35] S. Shimpalee, S. Greenway, D. Spuckler, J.W. Van Zee, Journal of Power Sources 158 (2004) 79–87.
[36] K.S. Dhathathreyan, P. Sridhar, G. Sasikumar, K.K. Ghosh, G. Velayutham, N. Rajalakshmi, C.K. Subramaniam, M. Raja, K. Ramya, International Journal of Hydrogen Energy 24 (1999) 1107–1115.
[37] K. Jiao, Experimental and modelling studies of cold start processes in proton exchange membrane fuel cells, Ph.D. thesis, University of Waterloo, 2011.